Quasinormal modes in nonlinear σ models in the Eddington inspired Born-Infeld gravity

Bobir Toshmatov,[1,2,*] Bobomurat Ahmedov,[2,3,4,†] Azamjon Boydedayev,[2,‡] and Sardor Tojiev[2,§]

[1]*New Uzbekistan University, Movarounnahr str. 1, Tashkent 100000, Uzbekistan*
[2]*Ulugh Beg Astronomical Institute, Astronomy str. 33, Tashkent 100052, Uzbekistan*
[3]*Institute of Theoretical Physics, National University of Uzbekistan, Tashkent 100174, Uzbekistan*
[4]*Institute of Fundamental and Applied Research, "TIIAME" National Research University, Kori Niyoziy 39, Tashkent 100000, Uzbekistan*

(Received 6 November 2023; accepted 9 January 2024; published 1 February 2024)

In this paper we explore properties of the spacetime of the monopole in nonlinear σ-models in the Eddington inspired Born-Infeld gravity. Particularly, we examine the radii of characteristic circular orbits of the test particles such as the circular null geodesics, marginally bound and stable circular orbits as a function of the spacetime parameters. Furthermore, we explore the dynamics of the massless scalar field. To enhance the precision of calculations, we employ multiple methods, including the WKB (Wentzel-Kramers-Brillouin) approximation, asymptotic iteration, and continued fractions methods. Our calculations demonstrate that the scalar field within the field of the monopole under examination remains stable against scalar perturbations. Notably, variations in the monopole parameter influence the longevity of the damping time of perturbations, with smaller damping rates prolonging their existence.

DOI: 10.1103/PhysRevD.109.044003

I. INTRODUCTION

One of the most important challenges of contemporary theoretical physics lies in reconciling two fundamental theories of the field: Einstein's general relativity and the standard model of particle physics. Each of these theories has achieved significant success in their respective domains. A potential avenue for addressing this challenge involves exploring the concept of spontaneous symmetry breaking, a central phenomenon in particle physics. This phenomenon results in the formation of topological defects, such as cosmic strings, local and global monopoles, and domain walls [1–3]. It is noteworthy that, while domain walls and local monopoles are ruled out by observational data [4], data from the anisotropy of the cosmic microwave background [5–8] and data from the gravitational wave signal detected by the LIGO and Virgo scientific collaboration [9] impose stringent constraints on the free parameters of models involving these defects. The solution describing the spacetime geometry outside a global monopole core, as initially derived by Barriola and Vilenkin [10], offers a straightforward illustration. This solution is based on a triplet of scalar fields featuring a global $O(3)$ symmetry that spontaneously breaks down to $U(1)$, making it a fundamental and simple example. This can be understood in physical terms as follows: if a global monopole is captured by the Schwarzschild black hole, the resulting spacetime of the black hole presents a solid angle deficit, characteristic for the topological charge as described by the solution presented in [10].

While general relativity has exhibited remarkable accuracy in astrophysical scenarios, particularly in weak field approximations such as Solar System tests and post-Newtonian approximations [11], the quest for a comprehensive understanding of gravity prompts exploration into alternative and modified theories. This exploration is motivated by the absence of definitive evidence validating the adequacy of general relativity in the strong gravitational field regime and its ability to account for various cosmological phenomena. In particular, the need to reconcile observations with the theoretical framework of GR has led to the consideration of new unknown forms of matter, such as dark energy. Within the GR framework, the presence of dark energy is essential, as evidenced by its role in scenarios like cosmic inflation, where the energy-momentum tensor must exhibit negative pressures to drive inflationary expansion. Furthermore, the detection of gravitational waves resulting from the merger of binary black holes or neutron stars in binaries such as [12–16] detected by the LIGO and Virgo scientific collaborations and obtained images depicting supermassive black holes situated at the cores of the Milky Way [17] and elliptical M87 [18] galaxies accomplished by the Event Horizon Telescope

*toshmatov@astrin.uz
†ahmedov@astrin.uz
‡boydedayev@astrin.uz
§sardor@astrin.uz

(EHT) project have still left some room for the alternative and modified theories of gravity. It is well known that like the case in the gravitational wave signal, the temporal evolution of black hole perturbations can be categorized into three distinct phases: the initial burst of perturbations, the subsequent ringdown phase, and the protracted late-time tails of perturbations. [19–21]. The most important phase of this signal is the ringdown which is dominated by the wave with quasinormal modes that carry the information about the black hole parameters. In this paper we consider the Eddington inspired Born-Infeld (EiBI) gravity [22]. Being a modification of general relativity, the EiBI gravity introduces nonlinearity into the Einstein-Hilbert action, allowing for different gravitational dynamics. This theory has been extensively studied in both strong gravitational field regime and cosmological scales over time [23–26]. Recently, in the paper by Nascimento *et al.* [27] within the framework of the nonlinear σ-models minimally coupled to the EiBI gravity, they presented a new set of solutions for different σ-models. By adopting one of these solutions, we study the main characteristic circular orbits and related quantities, scalar perturbation in the chosen background and its evolution in time. The structure of this paper is as follows: In Sec. II, we introduce the spacetime model employed in our study and provide brief information on its main properties. In Sec. III we study obtain equations of motion for the test particle and calculate radii of the characteristic circular orbits. Sections IV and V are dedicated to the analysis of scalar perturbation evolution within the specified spacetime. We also employ various numerical methods to compute the characteristic frequencies of the ringdown phase for these perturbations. Additionally, Sec. VI focuses on the computation of quasinormal modes for the scalar field in a high-energy regime. Finally, in Sec. VII we summarize the main results obtained throughout the paper. Throughout the paper, we adopt the metric signature $(-,+,+,+)$ and set the speed of light and the Newtonian gravitational constant equal to the unity, $c = G = 1$.

II. BASIC EQUATIONS

The action of the EiBI gravity is given by

$$S = \frac{1}{8\pi\epsilon}\int d^4x\left[\sqrt{-\det\left(g_{\mu\nu}+\epsilon R_{(\mu\nu)}(\Gamma)\right)} - \sqrt{-\det(g_{\mu\nu})}\right] + S_m(g_{\mu\nu},\Phi), \tag{1}$$

where the parameter ϵ possesses an area dimension and governs the extent of nonlinearity within the theory and the Ricci tensor $R(\Gamma)$ is symmetrically arranged to prevent the emergence of ghostlike degrees of freedom [28]. This construction is based on the assumption that the connection Γ remains independent of the metric $g_{\mu\nu}$. The last term of the action, $S_m(g_{\mu\nu},\Phi)$, represents the action of the matter field Φ. This model has received thorough examination in the work by Nascimento *et al.* [27]. Specifically, in the context of the global monopole, novel solutions were derived. The action of the global monopole is given as

$$S_m = \int d^4x\sqrt{-g}\left[-\frac{1}{2}\partial_\mu\vec{\Phi}\partial^\mu\vec{\Phi} - \frac{\lambda}{4}\left(\vec{\Phi}\cdot\vec{\Phi}-\eta^2\right)^2\right], \tag{2}$$

where $\vec{\Phi}\equiv\Phi^i$ is a triplet of real scalar fields with $i = 1, 2, 3$. The model (2) exhibits spontaneous symmetry breaking in the transformation $O(3)\to U(1)$. The parameters λ and η are the coupling constant and the energy scale of the symmetry breaking, respectively. Within this framework new spherically symmetric, static monopole solution was obtained whose line element in the spherical coordinates (r,θ,ϕ) is given as

$$ds^2 = -\left(1-k^2\eta^2-\frac{2M_0}{\sqrt{r^2+\epsilon k^2\eta^2}}\right)dt^2 + \frac{r^2}{r^2+\epsilon k^2\eta^2}\times\left(1-k^2\eta^2-\frac{2M_0}{\sqrt{r^2+\epsilon k^2\eta^2}}\right)^{-1}dr^2 + r^2d\Omega^2, \tag{3}$$

with $k^2 = 8\pi$, $d\Omega^2 = d\theta^2+\sin^2\theta d\phi^2$. One can easily notice from the line element (3) that if $\epsilon = 0$, it reduces to the well-known global monopole solution in general relativity [10,29]. By introducing the following new variables

$$k\eta\to\eta, \qquad r\to\sqrt{x^2-\epsilon\eta^2}, \tag{4}$$

the line element (3) can be rewritten as

$$ds^2 = -f(x)dt^2 + \frac{dx^2}{f(x)} + (x^2-\epsilon\eta^2)d\Omega^2, \tag{5}$$

with

$$f(x) = 1-\eta^2-\frac{2M_0}{x}. \tag{6}$$

The spacetime (5) with metric function (6) has a coordinate singularity at

$$x_0 = \frac{2M}{1-\eta^2}, \tag{7}$$

and the curvature singularity at

$$x = \eta\sqrt{\epsilon}. \tag{8}$$

III. CHARACTERISTIC CIRCULAR ORBITS

In this section, we briefly show the characteristic circular orbits around k-monopole in the EiBI gravity. One must note here that if the spacetime (5) with metric function (6) were to describe the monopole alone, there would be a noticeable deficit solid angle, signifying that the area of the sphere with radius r is less than $4\pi r^2$. This, in turn, would induce various nontrivial alterations to the orbit around the monopole, including effects like precession and distortion of circular orbits, among others. However, when considering the scenario where the mass of the black hole is significantly larger than the size of the monopole ($M \gg \delta$), as emphasized in [10,30], it is plausible to assume that the black hole with mass M has swallowed the monopole. In our paper, we specifically considered this latter case.

The initial step is to derive the equations of motion for the test particle in the gravitational field of the k-monopole (5). For simplicity, we assume that the particle's motion is restricted to the equatorial plane ($\theta = \pi/2$). Notably, the symmetry of the spacetime metric (5) leads to the conservation of the particle's momenta corresponding to the time and azimuthal coordinates. These conserved momenta are identified as the energy, denoted as E, and angular momentum, denoted as L, of the particle, respectively, as

$$f(x)u^t = E, \qquad (x^2 - \epsilon\eta^2)u^\phi = L. \tag{9}$$

Moreover, from the conservation of energy (normalization condition) $u^\mu u_\mu = -\delta$, we can find the only remaining component of the 4-momentum, u^x, as

$$(u^x)^2 = E^2 - V_{\text{eff}}, \qquad V_{\text{eff}} = f(x)\left(\frac{L^2}{x^2 - \epsilon\eta^2} + \delta\right). \tag{10}$$

where δ corresponds to 0 and -1 for the massless and massive particles, respectively. As we stated earlier we are interested in only the circular orbits in this section. The effective potential (10) for the massive test particle has a barrier-like shape which is zero at the spacetime singularity, r_+, and asymptotically tends to $1-\eta^2$ at spatial infinity. It is well known that the particle moving along the circular orbit has zero radial velocity ($u^x = 0$) and acceleration ($Du^x/d\tau$). By using these conditions, one can find the energy and angular momentum of the particle as

$$E = \frac{\sqrt{x}(2M - (1-\eta^2)x)}{\sqrt{(1-\eta^2)x^3 - M(3x^2 - \eta^2\epsilon)}}, \tag{11}$$

$$L = \frac{\sqrt{M}(x^2 - \eta^2\epsilon)}{\sqrt{(1-\eta^2)x^3 - M(3x^2 - \eta^2\epsilon)}}. \tag{12}$$

From the divergence of the energy of the particle at the photon sphere, we can easily notice that the photon sphere is determined by the solution of the following equation:

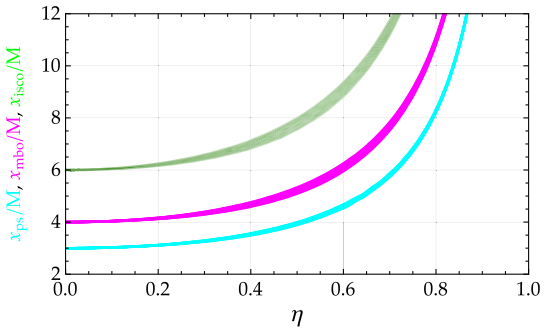

FIG. 1. Dependence of radii of the photon sphere (cyan), marginally bound orbit (magenta) and ISCO (green) on the spacetime parameters in the range of $\epsilon \in [0, 5]$. Where $\epsilon = 0$ corresponds to the upper border of regions.

$$(1-\eta^2)x_{\text{ps}}^3 - 3Mx_{\text{ps}}^2 + \eta^2\epsilon M = 0. \tag{13}$$

One more interesting orbit is the so-called marginally bound orbit which is determined by the asymptotic value of the energy at infinity as $E = 1 - \eta^2$ that gives

$$x_{\text{mbo}} = \frac{2M + \sqrt{4M^2 - \eta^2\epsilon(1-\eta^2)^2}}{1-\eta^2}. \tag{14}$$

One more astrophysically important orbit is the innermost stable circular orbit (ISCO) which is the closest distance at which a particle can stably orbit the black hole in a circular path.

$$2M(3x_{\text{isco}}^2 + \eta^2\epsilon) - (1-\eta^2)(x_{\text{isco}}^2 + 3\eta^2\epsilon)x_{\text{isco}} = 0, \tag{15}$$

We present the dependence of the radii of the characteristic circular orbits on the spacetime parameters in Fig. 1. It is evident from the figure that the photon sphere radius increases as the monopole parameter η grows, although it exhibits a slight decrease with increasing the value of ϵ, as demonstrated in [31,32]. Similar observations apply to the other circular orbits, including the marginally bound orbit and ISCO. We would also like to present another essential quantity in our analysis, which is the binding energy of a particle following the trajectory of the ISCO. This binding energy provides insight into the potential energy release during the accretion process. As our spacetime is asymptotically nonflat, approaching $1-\eta^2$ at spatial infinity, the binding energy is determined using the formula $E_{\text{bind}} = \sqrt{1-\eta^2} - E_{\text{isco}}$. The outcomes are illustrated in Fig. 2, showcasing variations across different spacetime parameter values. As it can be seen in Fig. 2, the binding energy exhibits a decreasing trend as the monopole parameter η increases, eventually converging to zero as η approaches 1. Similar to the characteristic orbits, the influence of the parameter ϵ on the binding energy of the particle orbiting along the ISCO is minimal.

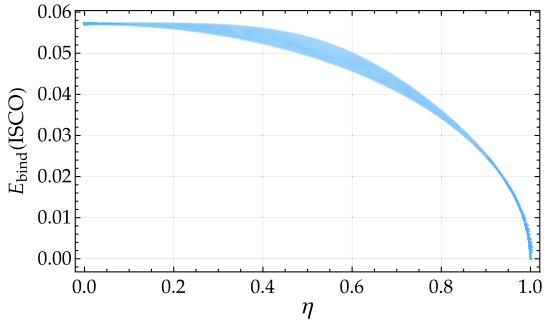

FIG. 2. Dependence of the binding energy of the particle moving along the ISCO on the spacetime parameters in the range of $\epsilon \in [0, 5]$. Where $\epsilon = 0$ corresponds to the lower border of regions.

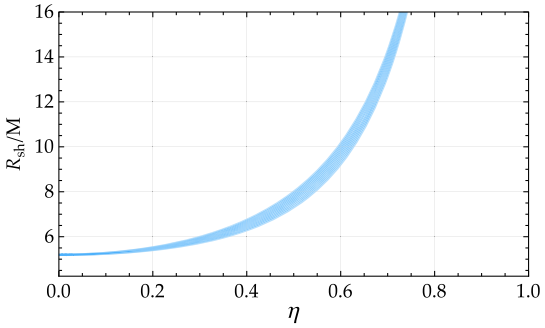

FIG. 3. Dependence of radii of the shadow on the spacetime parameters in the range of $\epsilon \in [0, 5]$. Where $\epsilon = 0$ corresponds to the upper border of regions.

Another crucial radius for observers is the shadow radius, representing the apparent size of the region around the black hole where no light can escape due to the black hole's powerful gravitational attraction. This shadow radius sometimes referred to as the critical impact parameter of a photon, can be computed by simplifying the right-hand side of the radial equation of motion of the photon into a polynomial form and setting the determinant of that polynomial equal to zero,[1] as demonstrated in previous works such as [33–35]. Thus, by doing so we obtain the following equation for the shadow radius:

$$27M^2R_{\rm sh}^4 + \left[(R_{\rm sh}^2 - \epsilon)\eta^2 - R_{\rm sh}^2\right]^3 = 0, \tag{17}$$

whose analytical solution has a cumbersome form. Given the complexity of the analytical form of the photon sphere, we present a visual representation of the dependence of the shadow radius on the spacetime parameters in Fig. 3. In the figure, it is evident that as the monopole parameter η approaches zero, the shadow radius converges to $R_{\rm sh} = 3\sqrt{3}M$, consistent with that of the Schwarzschild black hole. Conversely, as the monopole parameter η increases, the shadow radius also increases, and as η approaches one, it exhibits divergence. When considering a spacetime that deviates slightly from the Schwarzschild metric due to a small monopole parameter, the shadow radius can be expressed as follows

$$R_{\rm sh} = 3\sqrt{3}M + \frac{(27-\epsilon)\eta^2}{2\sqrt{3}}M + O(\eta^4). \tag{18}$$

[1]Or it can also be calculated via the following expression:

$$R_{\rm sh} = \sqrt{\frac{x_{\rm ps}^2 - \epsilon\eta^2}{f(x_{\rm ps})}}, \tag{16}$$

where the radius of the photon sphere is given by the greatest positive solution of Eq. (13).

On the other hand, the spacetime parameter ϵ always decreases the radius of the shadow but its effect is very small.

IV. SCALAR FIELD

In this section, we consider the test scalar field in the field of the monopole given by (5) with metric function (6). The general relativistic Klein-Gordon equation for the massless scalar field Ψ is given by

$$g^{\mu\nu}\nabla_\mu\nabla_\nu\Psi(t, x, \theta, \phi) = 0. \tag{19}$$

To separate angular variables in the Klein-Gordon equation (19), we represent the scalar field in terms of the spherical harmonics as

$$\Psi(t, x, \theta, \phi) = R(t, x)Y_\ell(\theta, \phi), \tag{20}$$

and obtain the following equation for the function R:

$$-\frac{1}{f^2}\frac{\partial^2 R}{\partial t^2} + \frac{\partial^2 R}{\partial x^2} + \left(\frac{f'}{f} + \frac{2x}{x^2 - \eta^2\epsilon}\right)\frac{\partial R}{\partial x} + \frac{L^2}{f(x^2 - \eta^2\epsilon)}R = 0, \tag{21}$$

where L^2 is the square of the total angular momentum operator whose explicit form is given by

$$L^2 = -\left[\frac{1}{\sin\theta}\frac{\partial}{\partial\theta}\left(\sin\theta\frac{\partial}{\partial\theta}\right) + \frac{1}{\sin^2\theta}\frac{\partial^2}{\partial\phi^2}\right]. \tag{22}$$

The eigenvalue of the square of the angular momentum operator is given by

$$L^2Y_\ell(\theta, \phi) = \ell(\ell + 1)Y_\ell(\theta, \phi), \tag{23}$$

where the value of the multipole number is within the range of $\ell = 0, 1, 2, \ldots$. Thus, the Eq. (21) can be rewritten as

$$-\frac{1}{f^2}\frac{\partial^2 R}{\partial t^2}+\frac{\partial^2 R}{\partial x^2}+\left(\frac{f'}{f}+\frac{2x}{x^2-\eta^2\epsilon}\right)\frac{\partial R}{\partial x}-\frac{\ell(\ell+1)}{f(x^2-\eta^2\epsilon)}R=0. \tag{24}$$

If the wave function is chosen as the following:

$$R(t,x)=\frac{\Psi(x,t)}{\sqrt{x^2-\eta^2\epsilon}}, \tag{25}$$

the wave equation (24) can be written as

$$-\frac{1}{f^2}\frac{\partial^2\Psi}{\partial t^2}+\frac{\partial^2\Psi}{\partial x^2}+\frac{f'}{f}\frac{\partial\Psi}{\partial x} -\left(\frac{\ell(\ell+1)}{f(x^2-\eta^2\epsilon)}-\frac{\eta^2\epsilon f-xf'(x^2-\eta^2\epsilon)}{f(x^2-\eta^2\epsilon)^2}\right)\Psi=0, \tag{26}$$

Now by introducing the "tortoise" coordinates instead of x as

$$dx_*=\frac{dx}{f}=\frac{2M\log\left((1-\eta^2)x-2M\right)+x(1-\eta^2)}{(1-\eta^2)^2}, \tag{27}$$

the wave equation (26) can be rewritten as

$$-\frac{\partial^2\Psi}{\partial t^2}+\frac{\partial^2\Psi}{\partial x_*^2}-V(x)\Psi=0, \tag{28}$$

the effective potential

$$V(x)=f\left[\frac{\ell(\ell+1)}{x^2-\eta^2\epsilon}-\frac{\eta^2\epsilon f-xf'(x^2-\eta^2\epsilon)}{(x^2-\eta^2\epsilon)^2}\right]. \tag{29}$$

If the dynamics of the scalar field is harmonically time dependent as $\Psi=\psi(x)\exp(-i\omega t)$, the wave equation (28) can be written in well-known Schrödinger-like form as

$$\frac{d^2\psi}{dx_*^2}+(\omega^2-V(x))\psi=0. \tag{30}$$

Behavior of the effective potential in the parametric space is analyzed in Fig. 4. It reveals that as usual the multipole number increases the height of the effective potential, while the spacetime parameter ϵ exhibits a similar impact, yet its influence remains comparatively less pronounced than that of the multipole number. On the other hand, the global monopole parameter η exerts a diminishing effect on the effective potential's height—see right panel of Fig. 4. At a certain value of η, the effective potential even loses its barrierlike configuration.

Below in the next sections, we solve the wave equation (30) with appropriate boundary conditions by using several methods.

V. QUASINORMAL MODES

In this section, by applying semi-analytical and numerical methods we solve the eigenvalue problem in Eq. (30).

A. WKB method

To solve the eigenvalue problem in the wave equation (30) with the effective potential (29), one must impose the boundary condition. Considering the form of the effective potential, which gradually approaches zero at spatial infinity and diminishes at the coordinate singularity of the spacetime, we opt for a waveform that aligns with these boundaries. Specifically, we select a waveform that exhibits purely incoming behavior at the coordinate singularity and purely outgoing behavior at spatial infinity, thereby achieving

$$\Psi(r)=\begin{cases} e^{-i\omega r_*} & \text{at } r_*\to-\infty, \quad \left(x\to\frac{2M}{1-\eta^2}\right), \\ e^{i\omega r_*} & \text{at } r_*\to\infty, \quad (x\to\infty). \end{cases} \tag{31}$$

We here adopt the Wentzel-Kramers-Brillouin (WKB) approximation method to calculate the quasinormal modes of the scalar field in the field of the monopole in the nonlinear σ-model in the EiBI gravity. The WKB method offers a powerful semi-analytical technique to approximate the complex frequencies of quasinormal modes. One must note that the WKB method is an approximate technique whose higher order corrections enhance its accuracy. This method was applied for calculations of quasinormal modes of black holes for the first time by Schutz and Will [36] and

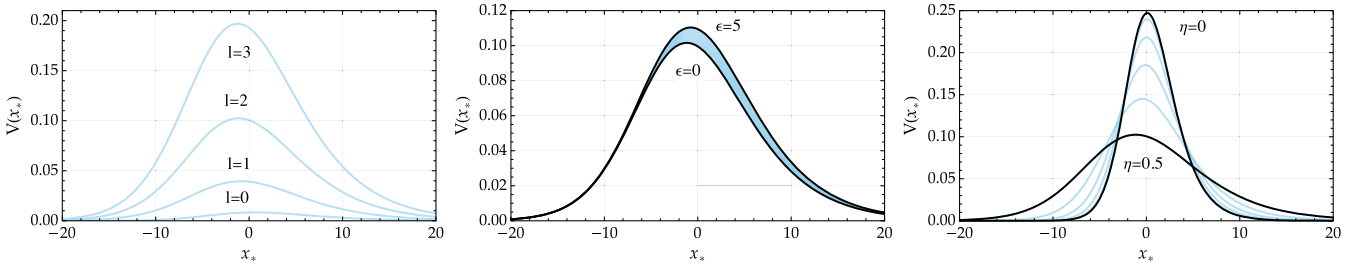

FIG. 4. The effective potential of the scalar field in the field of the k-monopole in the EiBI gravity as a function of the tortoise coordinate for various values of the spacetime and scalar field parameters. Left panel: $\eta=0.5$, $\epsilon=0.5$. Middle panel: $\ell=2$, $\epsilon=0.5$. Right panel: $\ell=2$, $\epsilon=0.5$.

afterward, it was extended up to the third by Iyer and Will [37,38] and to the sixth orders by Konoplya [39], respectively. It has recently been extended up to the thirteenth orders in terms of the Padé approximations by Matyjasek and Opala [40] as

$$\omega^2 = V_0 + A_2(\mathcal{K}^2) + A_4(\mathcal{K}^2) + A_6(\mathcal{K}^2) + \cdots - i\mathcal{K}\sqrt{-2V_2}\left[1 + A_3(\mathcal{K}^2) + A_5(\mathcal{K}^2) + A_7(\mathcal{K}^2)\ldots\right]. \tag{32}$$

where V_0 is the maximum value of the effective potential, $\mathcal{K}$ is a half-integer and $A_k(\mathcal{K}^2)$ are corrections terms with order k and polynomials in $\mathcal{K}^2$ with rational coefficients. As it has been pointed out in [41], the WKB method demonstrates poor accuracy or limited applicability in the following scenarios:

(i) Superradiance: this occurs when the rotation of a black hole results in an incident wave being reflected with increased amplitude. The WKB method struggles to accurately model such phenomena.
(ii) Black hole stability: the WKB method is adept at handling cases with positive effective potentials, giving rise to damping waves ($\omega_i < 0$). However, it is inadequate for cases featuring negative effective potentials, signifying instability ($\omega_i > 0$).
(iii) Infinitely long-lived mode (quasi-resonance mode): this mode corresponds to the case where the peak and asymptotic value of the effective potential are equal. The WKB method encounters challenges when dealing with these types of configurations.
(iv) Asymptotically nonconstant effective potentials: the WKB method encounters difficulties when addressing scenarios characterized by effective potentials that do not remain constant as they approach infinity.

It has very good accuracy in cases where the potential barrier that the perturbation experiences is deep and narrow. By examining the effective potential's shape for different values of spacetime and field parameters as illustrated in Fig. 4, we observe that as the values of the multipole ℓ and nonlinearity parameter ϵ increase, the effective potential's configuration becomes more suitable for the application of the WKB method. However, when the monopole parameter η increases, it results in a reduction in the height of the effective potential, consequently diminishing the accuracy of the WKB method.

B. Asymptotic iteration method

As mentioned earlier in a previous subsection, the accuracy of the WKB method depends upon the shape of the effective potential. As demonstrated in Fig. 4, it is evident that for certain values of the monopole parameter, the width of the effective potential increases, consequently leading to a decrease in the accuracy of the WKB method. Therefore, it becomes necessary to employ an additional calculation method alongside the WKB method to cross-verify and compare the results. Therefore, in this subsection we employ the improved asymptotic iteration method (AIM) [42–44]. The first we rewrite the wave equation (26) in terms of the new variable defined by $y = 1/x$ as

$$\psi'' + \frac{2f + yf'}{yf}\psi' + \left[\frac{\omega^2}{y^4 f^2} - \frac{\ell(\ell+1)}{y^2 f(1-\eta^2\epsilon y^2)} + \frac{\eta^2\epsilon y f - f'(1-\eta^2\epsilon y^2)}{yf(1-\eta^2\epsilon y^2)^2}\right]\psi = 0, \tag{33}$$

where the prime stands for the derivative with respect to y. Thus, one can rewrite the tortoise coordinate (27) in terms of the new variable y as

$$x_* = \frac{1 - \eta^2 + 2My\log\left(\frac{1-\eta^2}{y} - 2M\right)}{(1-\eta^2)^2 y}. \tag{34}$$

To avoid the divergence of the wave function at the spatial infinity ($y \to 0$), we choose the wave function in the following form:

$$\psi = e^{i\omega x_*}\xi(y), \tag{35}$$

and the wave equation (33) reduces to the following form in terms of the new variable ξ:

$$\xi'' + 2A\xi' + B\xi = 0, \tag{36}$$

where

$$A = \frac{1}{y(\eta^2 y^2\epsilon - 1)} + \frac{y(\eta^2 + 3My - 1) + i\omega}{y^2(\eta^2 + 2My - 1)},$$
$$B = \frac{2i\omega - \ell(\ell+1)y}{y^3(\eta^2 + 2My - 1)(\eta^2 y^2\epsilon - 1)}.$$

From the appropriate quasinormal condition at the spacetime singularity, we write the wave function as

$$\xi(y) = \left(y - \frac{1-\eta^2}{2M}\right)^{\frac{-i\omega}{\kappa}} u(y) \tag{37}$$

where the surface gravity is given by

$$\kappa = -\left.\frac{y^2 f'(y)}{2}\right|_{y=y_0} = \frac{(1-\eta^2)^2}{4M}. \tag{38}$$

By inserting the wave function (37) into the wave equation (36), we arrive at the following equation

$$u'' = \lambda_0 u' + s_0 u, \tag{39}$$

with

$$\lambda_0 = \frac{2}{\eta^2 + 2My - 1}\left(\frac{M - \eta^2 y\epsilon(\eta^2 + 3My - 1)}{\eta^2 y^2\epsilon - 1} - \frac{i\omega(\eta^2 + 4My - 1)}{(\eta^2 - 1)y^2}\right),$$
$$s_0 = \frac{(1-\eta^2)^2\ell(\ell+1)y - 2i(1-\eta^2)\omega(\eta^2 + 2M(\eta^2 y^3\epsilon + y) - 1) + 8M\omega^2(\eta^2 y^2\epsilon - 1)}{(1-\eta^2)^2 y^3(\eta^2 + 2My - 1)(\eta^2 y^2\epsilon - 1)}, \tag{40}$$

By taking $n-2$ successive derivatives of equation (39) with respect to y, we derive the following equation, as also demonstrated in [43,45]:

$$u^{(n+2)} = \lambda_n u' + s_n u, \tag{41}$$

with coefficients that adhere to the subsequent recurrent relations:

$$\lambda_n = \lambda'_{n-1} + s_{n-1} + \lambda_0\lambda_{n-1},$$
$$s_n = s'_{n-1} + s_0\lambda_{n-1}. \tag{42}$$

Now, we express the coefficients λ_n and s_n as Taylor series expansions around an arbitrary point y_0, given by:

$$\lambda_n = \sum_{i=0}^{\infty} c_n^i (y - y_0)^i,$$
$$s_n = \sum_{i=0}^{\infty} d_n^i (y - y_0)^i, \tag{43}$$

where c_n^i and d_n^i are the ith coefficients of λ_n and s_n, respectively, in the Taylor series. Upon substituting Eq. (43) into Eq. (53), we can derive the following expressions:

$$c_n^i = (i+1)c_{n-1}^{i+1} + d_{n-1}^i + \sum_{k=0}^{i} c_0^k c_{n-1}^{i-k},$$
$$d_n^i = (i+1)d_{n-1}^{i+1} + \sum_{k=0}^{i} d_0^k c_{n-1}^{i-k}. \tag{44}$$

For sufficiently large values of n, we can deduce the asymptotic behavior of the coefficients, as follows:

$$\frac{s_n}{\lambda_n} = \frac{s_{n-1}}{\lambda_{n-1}}. \tag{45}$$

Finally, we arrive at the subsequent recurrence relation, which is employed for the computation of quasinormal modes:

$$d_n^0 c_{n-1}^0 - c_n^0 d_{n-1}^0 = 0. \tag{46}$$

C. Continued fractions method

As shown in Table I, it is evident that the quasinormal frequencies derived from the WKB and AIM methods exhibit small discrepancies, especially for lower multipole numbers. In situations like these, it is often necessary to employ an additional third method to achieve greater precision in the results. Therefore, we adopted one of the most powerful semianalytical methods the continued fraction method (CFM) which was for the first time applied for calculations of quasinormal modes by Leaver [46], as a "judging" method. For simplicity of our further calculations, we rewrite the spacetime function in the following form:

$$f(x) = (1-\eta^2)\left(1 - \frac{x_0}{x}\right), \tag{47}$$

with x_0 being given by (7). In the CFM one must choose the appropriate eigenfunction for the wave equation (30) by using the boundary conditions. As we have earlier stated the wave behaves as purely incoming and outgoing at the horizon and spatial infinity, respectively. Since the effective potential (29) tends to zero at these two boundaries, it is now easier to construct the wave functions at these two boundaries. As the radial coordinate tends to the spacetime horizon, the tortoise coordinate tends to

$$x_* \simeq \frac{x_0}{1-\eta^2}\ln\left(1 - \frac{x_0}{x}\right), \tag{48}$$

appropriately, the purely incoming wave behaves as

$$\psi \simeq \left(1 - \frac{x_0}{x}\right)^{-\frac{i\omega x_0}{1-\eta^2}}. \tag{49}$$

The tortoise coordinate takes the following approximate form at spatial infinity:

$$x_* \simeq \frac{x}{1-\eta^2} + \frac{x_0}{1-\eta^2}\ln\left(\frac{x}{x_0}\right), \tag{50}$$

TABLE I. The fundamental quasinormal frequencies of the massive scalar field in the field of the k-monopole in the EiBI gravity calculated via the higher order WKB, asymptotic iteration (AIM), continued fraction (CFM) methods.

ℓ	η	ϵ	WKB	AIM	CFM
0	0	$\forall\epsilon$	0.113977–0.104657 i	0.110144–0.104590 i	0.116883–0.119653 i
	0.2	0	0.108809–0.100589 i	0.137340–0.129380 i	0.107719–0.110272 i
		0.2	0.103551–0.094857 i	0.131488–0.115088 i	0.107705–0.109679 i
		0.4	0.102399–0.093473 i	0.198790–0.132090 i	0.108189–0.108079 i
	0.5	0	0.064640–0.059476 i	0.049276–0.088492 i	0.065747–0.067305 i
		0.2	0.062279–0.056760 i	0.036026–0.021940 i	0.058931–0.074021 i
		0.4	0.062286–0.056754 i	0.035438–0.027183 i	0.055436–0.072879 i
1	0	$\forall\epsilon$	0.293038–0.097599 i	0.292936–0.097660 i	0.281262–0.095080 i
	0.2	0	0.274755–0.090046 i	0.290134–0.067925 i	0.266230–0.087437 i
		0.2	0.274844–0.089962 i	0.285558–0.064564 i	0.266645–0.087468 i
		0.4	0.274964–0.089968 i	0.302592–0.062463 i	0.266138–0.088152 i
	0.5	0	0.187015–0.054774 i	0.183869–0.053674 i	0.181928–0.052323 i
		0.2	0.187051–0.054842 i	0.201176–0.058622 i	0.181865–0.051651 i
		0.4	0.187659–0.054780 i	0.192605–0.055660 i	0.182512–0.051151 i
2	0	$\forall\epsilon$	0.483646–0.096757 i	0.483644–0.096759 i	0.478254–0.086764 i
	0.2	0	0.454478–0.089255 i	0.455114–0.089054 i	0.449770–0.079699 i
		0.2	0.454632–0.089169 i	0.455100–0.089040 i	0.450291–0.079508 i
		0.4	0.454458–0.089153 i	0.454971–0.089177 i	0.450612–0.079418 i
	0.5	0	0.312151–0.054261 i	0.311916–0.053815 i	0.310451–0.047751 i
		0.2	0.312659–0.054382 i	0.312685–0.054413 i	0.311323–0.047756 i
		0.4	0.313417–0.054423 i	0.313366–0.054564 i	0.311981–0.047775 i

and corresponding wave function behaves as

$$\psi \simeq \left(\frac{x}{x_0}\right)^{\frac{i\omega x_0}{1-\eta^2}} e^{\frac{i\omega x}{1-\eta^2}}. \tag{51}$$

By combining the waveforms at boundaries (49) and (51), we assume the eigenfunction of the wave equation (30) in the following series form:

$$\psi = \left(\frac{x}{x_0}\right)^{\frac{i\omega x_0}{1-\eta^2}} \left(1-\frac{x_0}{x}\right)^{\frac{i\omega x_0}{\eta^2-1}} e^{\frac{i\omega x}{1-\eta^2}} \sum_{n=1}^{\infty} a_n \left(1-\frac{x_0}{x}\right)^n, \tag{52}$$

By inserting the wave function (52) to the equation (26) and extracting the homogeneous terms with respect to $1-x_0/x$, one obtains the following seven-term recurrence relation:

$$\begin{aligned}
\alpha_n a_{n+1} + \beta_n a_n + \gamma_n a_{n-1} + \delta_n a_{n-2} + \epsilon_n a_{n-3} + \theta_n a_{n-4} + \xi_n a_{n-5} &= 0, \qquad n \geq 5, \\
\alpha_4 a_5 + \beta_4 a_4 + \gamma_4 a_3 + \delta_4 a_2 + \epsilon_4 a_1 + \theta_4 a_0 &= 0, \\
\alpha_3 a_4 + \beta_3 a_3 + \gamma_3 a_2 + \delta_3 a_1 + \epsilon_3 a_0 &= 0, \\
\alpha_2 a_3 + \beta_2 a_2 + \gamma_2 a_1 + \delta_2 a_0 &= 0, \\
\alpha_1 a_2 + \beta_1 a_1 + \gamma_1 a_0 &= 0, \\
\alpha_0 a_1 + \beta_0 a_0 &= 0,
\end{aligned} \tag{53}$$

where

$$\alpha_n = (1-\eta^2)(n+1)(x_0^3-\eta^2 x_0\epsilon)^2((\eta^2-1)(n+1)+2ix_0\omega),$$
$$\beta_n = x_0^2(\eta^2\epsilon-x_0^2)\{2\eta^2(\eta^2-1)^2n(3n+1)\epsilon + x_0[x_0((\eta^2-1)(l^2+l-(\eta^2-1)(2n(n+1)+1)) + 4x_0\omega(2x_0\omega - i(\eta^2-1)(2n+1)) - 8\eta^2\omega^2\epsilon) + 4i(\eta^2-1)\eta^2(4n+1)\omega\epsilon]\},$$
$$\gamma_n = x_0^2\{-5\eta^4(\eta^2-1)^2(n-1)(3n-1)\epsilon^2 + x_0[x_0(-2(\eta^2-1)\eta^2\epsilon(l^2+l-(\eta^2-1)(6(n-1)n+1)) + x_0^2((\eta^2-1)^2(-n^2) + 4x_0\omega(x_0\omega - i(\eta^2-1)n) - 40\eta^2\omega^2\epsilon) + 4i(\eta^2-1)\eta^2(11n-5)x_0\omega\epsilon + 36\eta^4\omega^2\epsilon^2) - 4i\eta^4(\eta^2-1)(12n-7)\omega\epsilon^2]\},$$
$$\delta_n = \eta^2x_0^2\epsilon\{20\eta^2(\eta^2-1)^2(n-2)(n-1)\epsilon + x_0[x_0((\eta^2-1)(l^2+l-(\eta^2-1)(4n(2n-5)+9)) + 8x_0\omega(4x_0\omega - i(\eta^2-1)(4n-5)) - 64\eta^2\omega^2\epsilon) + 8i(\eta^2-1)\eta^2(9n-13)\omega\epsilon]\}$$
$$\epsilon_n = \eta^2x_0^2\epsilon[(\eta^2-1)(n-3)+2ix_0\omega][2(\eta^2-1)(n-1)x_0^2 - 5\eta^2(\eta^2-1)(3n-5)\epsilon + 4ix_0^3\omega - 28i\eta^2x_0\omega\epsilon],$$
$$\theta_n = 2\eta^4x_0^2\epsilon^2[(\eta^2-1)(n-4)+2ix_0\omega][(\eta^2-1)(3n-7)+6ix_0\omega],$$
$$\xi_n = -\eta^4x_0^2\epsilon^2[(\eta^2-1)(n-5)+2ix_0\omega][(\eta^2-1)(n-3)+2ix_0\omega].$$

In the case of the recurrence relations that involve more than three expansion coefficients a_n, as is the case here, Leaver's method for solving such relations cannot be applied directly. Instead, we should first use the Gaussian elimination method to gradually reduce the initial seven-term recurrence relation to a three-term recurrence relation [47,48]. Here to reduce the seven-term recurrence relation (53) to the three-term recurrence relation, one applies the Gauss elimination procedure 4 times in a row and eventually obtains the following three-term recurrence relation:

$$\alpha_n^{(4)}a_{n+1} + \beta_n^{(4)}a_n + \gamma_n^{(4)}a_{n-1} = 0, \quad n \geq 1,$$
$$\alpha_0^{(4)}a_1 + \beta_0^{(4)}a_0 = 0, \tag{54}$$

where $z^{(4)}$ stands for the coefficient z after four times application of the Gaussian elimination procedure and for $n \geq 2$

$$\alpha_n^{(4)} = \alpha_n^{(3)} = \alpha_n^{(2)} = \alpha_n^{(1)} = \alpha_n,$$
$$\beta_n^{(4)} = \beta_n^{(3)} - \frac{\alpha_{n-1}^{(2)}}{\gamma_{n-1}^{(1)}}\delta_n^{(3)}, \qquad \gamma_n^{(4)} = \gamma_n^{(3)} - \frac{\beta_{n-1}^{(4)}}{\gamma_{n-1}^{(4)}}\delta_n^{(3)}, \tag{55}$$

Here we do not report the full expressions of the coefficients of the three-term recurrence relation (54), since the numerical procedure to obtain them is relatively simple. To solve the three-term recurrence relation, one needs to solve the following equation:

$$\beta_n^{(4)} - \frac{\alpha_{n-1}^{(4)}\gamma_n^{(4)}}{\beta_{n-1}^{(4)} - \frac{\alpha_{n-2}^{(4)}\gamma_{n-1}^{(4)}}{\beta_{n-2}^{(4)} - \alpha_{n-3}^{(4)}\gamma_{n-2}^{(4)}/\ldots}} = \frac{\alpha_n^{(4)}\gamma_{n+1}^{(4)}}{\beta_{n+1}^{(4)} - \frac{\alpha_{n+1}^{(4)}\gamma_{n+2}^{(4)}}{\beta_{n+2}^{(4)} - \alpha_{n+2}^{(4)}\gamma_{n+3}^{(4)}/\ldots}}. \tag{56}$$

Hence, the final column in Table I displays the quasinormal frequencies computed using Leaver's continued fraction method. An analysis of the results in Table I and Fig. 5 reveals a consistent trend: as the multipole number increases, so does the frequency of the actual oscillations in the perturbations. A similar effect is observed with respect to the spacetime parameter ϵ, though its impact remains relatively minor. Conversely, the k-monopole parameter η contributes to a decrease in the real part of the quasinormal frequencies. These behaviors are also evident when examining the effects of these parameters on the effective potential, as illustrated in Fig. 4.

D. Time evolution of scalar perturbation

In this section, we analyze the temporal evolution of the scalar field in the field of the k-monopole in the EiBI gravity. To do so, we adopt a characteristic integration method [49,50] and mostly follow the algorithm presented in [51] to present the formalism. This method utilizes light-cone variables, including the retarded time coordinate $du \equiv dt - dx_*$ and the advanced time coordinate $dv \equiv dt + dx_*$. Initial data is provided on the two null surfaces $u = u_0$ and $v = v_0$. Consequently, the wave equation (28) can be expressed as follows:

$$-4\frac{\partial^2\Psi}{\partial u\partial v} = V(r(u,v))\Psi. \tag{57}$$

Solving this equation necessitates the use of numerical methods. We partition the (u, v) space into a finite grid with a uniform spacing of Δ between adjacent grid points, as illustrated in Fig. 6. The employed numerical scheme for solving this equation is as follows:

$$\Psi_N = (\Psi_W + \Psi_E)\frac{16-\Delta^2V_S}{16+\Delta^2V_S} - \Psi_S + O(\Delta^4), \tag{58}$$

where the indices N, W, E, and S refer to grid-points $N \equiv (u, v)$, $W \equiv (u-\Delta, v)$, $E \equiv (u, v-\Delta)$, and $S \equiv (u-\Delta, v-\Delta)$. In our simulations, the initial perturbation

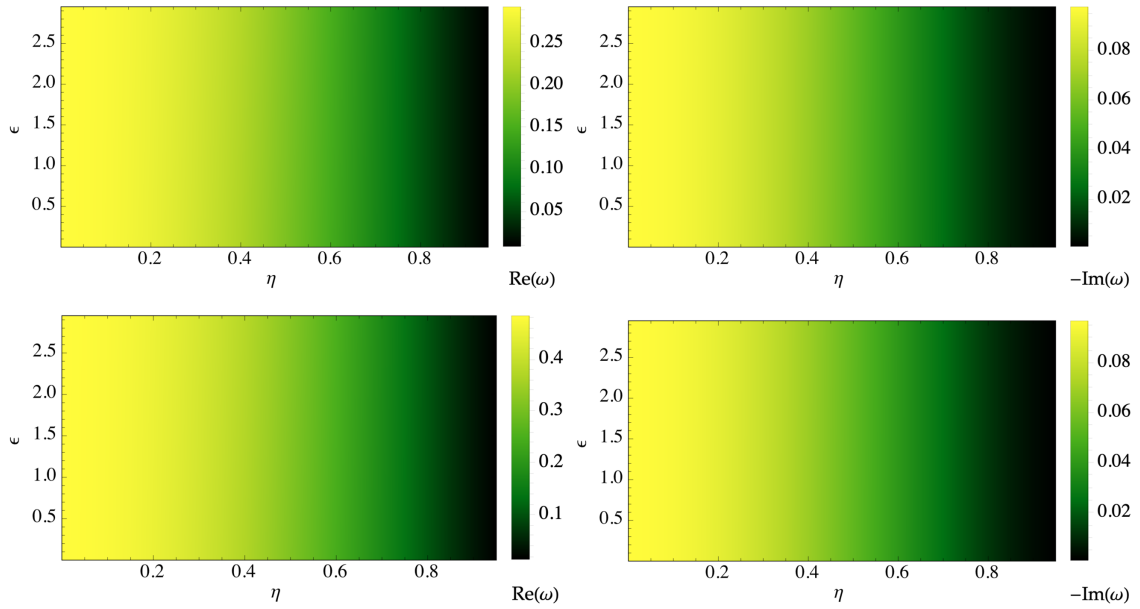

FIG. 5. The fundamental quasinormal frequencies of the scalar field with $\ell = 1$ (top panel) and $\ell = 2$ (bottom panel) in the field of the k-monopole for the spacetime parameters in the range of $\eta \in [0, 1]$ and $\epsilon \in [0, 3]$.

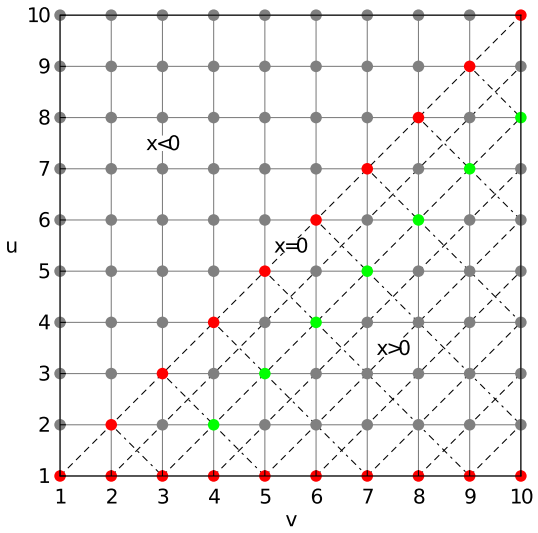

FIG. 6. The discretization scheme in the plane of (u, v) coordinates. The initial and boundary values are depicted by the red dots, where the horizontal ones signify initial values, and the diagonal ones represent boundary values. Meanwhile, the dashed lines indicate a constant coordinate at x_*, while the dot-dashed lines correspond to a constant coordinate at t. Within this context, the green dots represent the solution at a selected, unchanging coordinate point x_*. Credit to [51] for the scheme.

is a Gaussian function centered around the point x_{*c} and it takes the form

$$\Psi(t = 0, x_*) = A \exp\left(-(x_* - x_{*c})^2/\sigma^2\right) = A \exp\left(-(v - v_c)^2/\sigma^2\right) \tag{59}$$

since

$$t = 0 = \frac{1}{2}(u + v) \Rightarrow u = -v \tag{60}$$

and therefore

$$x_* = \frac{1}{2}(v - u) = v \tag{61}$$

for $t = 0$. At the center of the body, $x_* = 0$, we initially put the boundary condition $\Phi(u, v) = 0$ which is considered along the line $u = v$ since for

$$x_* = 0 = \frac{1}{2}(v - u) \Rightarrow u = v. \tag{62}$$

Our tortoise coordinate x_* is determined from the formula

$$x_* = \int_0^x \frac{1}{f(x')} \mathrm{d}x' \tag{63}$$

which implies that $x_* \geq 0$ for $x \geq 0$. We are therefore interested only in the region where $v \geq u$. In the integration loop the coordinates u and v are determined by formulas

$$u = i_u \Delta, \quad \text{where } i_u = \{1, 2, \ldots, N\}, \tag{64}$$

and

$$v = i_v \Delta, \quad \text{where } i_v = \{i_u + 1, i_u + 2, \ldots, N\}. \tag{65}$$

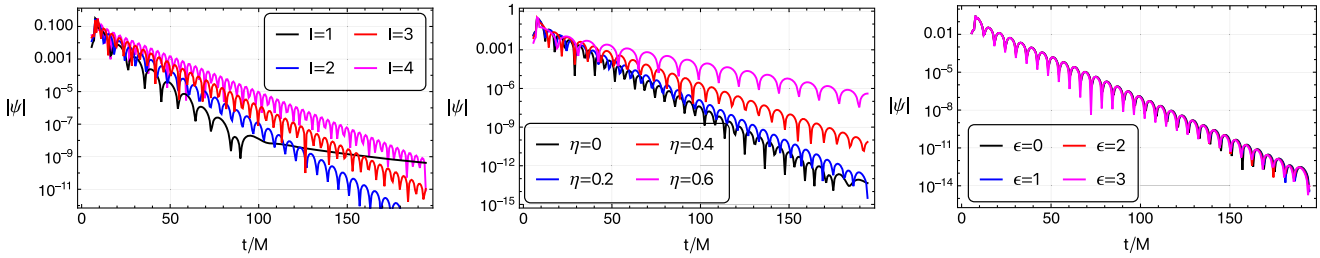

FIG. 7. Time-domain profile of the scalar perturbations in the field of the k-monopole in the EiBI gravity for various values of the spacetime and scalar field parameters. Left panel: $\eta = 0.2$, $\epsilon = 0.2$. Middle panel: $\ell = 2$, $\epsilon = 0.2$. Right panel: $\ell = 2$, $\eta = 0.2$.

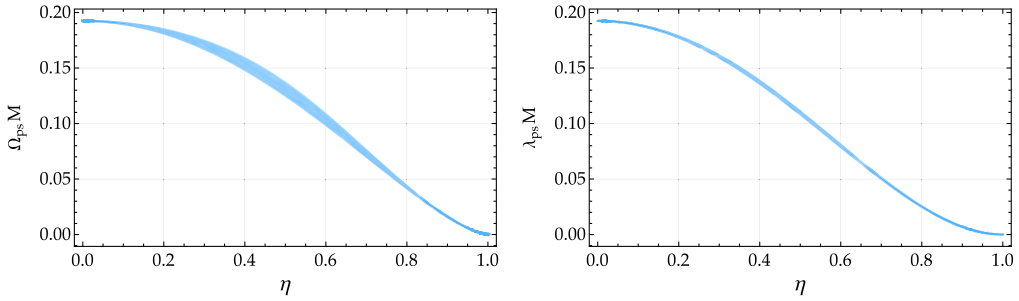

FIG. 8. The angular velocity and Lyapunov exponent of the circular null geodesics around k-monopole in the EiBI gravity as a function of η for the spacetime parameter ϵ in the range $\epsilon \in [0, 3]$. Where $\epsilon = 0$ corresponds to the lower boundary of the regions.

Thus, by utilizing the discretization approach outlined above, we solve the wave equation by inputting specific spacetime and field parameters. Some of these results are visualized in Fig. 7. This figure reaffirms the findings regarding the influence of spacetime and field parameters on scalar field evolution, as previously presented in Table I. Specifically, it highlights how variations in the multipole number consistently lead to higher frequencies and reduced damping rates of real oscillations. Conversely, the monopole parameter η tends to decrease both the frequency and damping rate of these oscillations. However, the influence of the spacetime parameter ϵ appears to be less significant in comparison.

VI. HIGH ENERGY REGIME

In this section, we consider the quasinormal modes of scalar perturbations around k-monopole in the EiBI gravity in the eikonal regime. The eikonal regime is defined by the high multipole number of the scalar field. As we have seen from the effective potential an increase in the value of the multipole number increases the height of the effective potential which implies us to consider the high energy regime. As the energy of the scalar field increases, its wavelength decreases and becomes almost negligible relative to the horizon scale of the black hole. Therefore, in this regime, massless scalar waves propagate along the null geodesics [52]. In the high values of the angular momentum (multipole number), the effective potential of the scalar perturbation (29) behaves as

$$V(x) = \ell^2\left[\frac{f(x)}{x^2 - \epsilon\eta^2} + O(\ell^{-1})\right], \tag{66}$$

where the leading term represents the effective potential for the massless particle (10). Through this relation, it has been shown in [53] that the quasinormal modes of perturbations of black holes in the eikonal regime can be described in terms of the angular velocity, $\Omega_{\rm ps}$, and Lyapunov exponent, $\lambda_{\rm ps}$, of the circular null geodesics[2] as

$$\omega = \Omega_{\rm ps}\ell - \left(n + \frac{1}{2}\right)|\lambda_{\rm ps}|, \tag{67}$$

where

$$\Omega_{\rm ps} = \frac{\dot{\phi}}{\dot{t}} = \sqrt{\frac{f(x_{\rm ps})}{2x_{\rm ps}}}, \tag{68}$$

and

$$\lambda_{\rm ps} = \sqrt{\frac{f(x_{\rm ps})[2f(x_{\rm ps}) - f''(x_{\rm ps})(x_{\rm ps}^2 - \epsilon\eta^2)]}{2(x_{\rm ps}^2 - \epsilon\eta^2)}}. \tag{69}$$

[2]It was shown in [54–57] it is not always the case, as in some spacetimes, the quasinormal modes of perturbations in the eikonal regime can be determined by the quantities characterizing the circular photon orbit, instead of the circular null geodesics.

In Fig. 8, we have depicted the variations of these characteristic quantities with respect to changes in the spacetime parameters. Notably, as shown in Fig. 8, both Ω_{ps} and λ_{ps} exhibit a decreasing behavior as the monopole parameter η increases, ultimately reaching zero at $\eta = 1$. The spacetime parameter ϵ does not significantly affect these quantities. From these observations, we can draw the following conclusions. Scalar waves emitted by the k-monopole in the context of EiBI gravity, especially with higher multipoles, exhibit reduced damping. This reduction is advantageous for their detectability. However, it is worth noting that these waves also possess longer wavelengths, which can make them more challenging to detect when compared to waves originating from a Schwarzschild black hole.

VII. CONCLUSION

In this paper, we considered the spacetime of the k-monopole in nonlinear σ-models in the EiBI gravity. Particularly, we examined the radii of characteristic circular orbits of the test particles such as the circular null geodesics, shadow of the k-monopole, marginally bound (MBO) and stable circular orbits (ISCO) as a function of the spacetime parameters. Calculations have revealed that as the monopole parameter's value increases, the radii of these orbits also experience an increase. Conversely, the nonlinearity parameter ϵ impacts these radii in the opposite direction, striving to reduce them, albeit with a minimal effect. Thus, in terms of the spacetime parameters, one can deduce that the monopole parameter strengthens, while the spacetime nonlinearity parameter slightly weakens the gravitational attraction of the spacetime. Moreover, we showed that the binding energy of the particle moving along the ISCO that represents the maximum potential energy release during the accretion process decreases with increasing the value of the monopole parameter in comparison with the one around the Schwarzschild black hole.

In addition to the characteristic circular orbits and related properties mentioned above, we explored the dynamics of the massless scalar field which is governed by the Klein-Gordon equation around k-monopole. By taking into account the spacetime symmetry and considering the scalar field is harmonically time dependent, we have divided variables in the field equation and obtained well-known Schrödinger-like wave equation with appropriate effective potential. By applying the appropriate boundary conditions at coordinate singularity and spatial infinity, we solved the eigenvalue problem that provides the quasinormal frequencies of the scalar field. To enhance the precision of calculations, we employed multiple methods, including the WKB approximation, asymptotic iteration and Leaver's continued fractions methods. Our calculations demonstrated that the scalar field within the field of the k-monopole under examination remains stable against scalar perturbations. Notably, variations in the monopole parameter influence the longevity of the damping time of perturbations, with smaller damping rates prolonging their existence.

ACKNOWLEDGMENTS

The authors acknowledge the support of the Ministry of Higher Education, Science and Innovation of the Republic of Uzbekistan Grants No. F-FA-2021-510, No. F-FA-2021-432, and No. MRB-2021-527.

[1] T. W. B. Kibble, J. Phys. A **9**, 1387 (1976).
[2] A. Vilenkin, Phys. Rep. **121**, 263 (1985).
[3] A. Vilenkin and E. P. S. Shellard, *Cosmic Strings and Other Topological Defects* (Cambridge University Press, Cambridge, 2000).
[4] P. P. Avelino, C. J. A. P. Martins, J. Menezes, R. Menezes, and J. C. R. E. Oliveira, Phys. Rev. D **78**, 103508 (2008).
[5] T. Charnock, A. Avgoustidis, E. J. Copeland, and A. Moss, Phys. Rev. D **93**, 123503 (2016).
[6] R. Brandenberger, B. Cyr, and R. Shi, J. Cosmol. Astropart. Phys. 09 (2019) 009.
[7] D. P. Bennett and S. H. Rhie, Astrophys. J. Lett. **406**, L7 (1993).
[8] A. Lopez-Eiguren, J. Lizarraga, M. Hindmarsh, and J. Urrestilla, J. Cosmol. Astropart. Phys. 07 (2017) 026.
[9] R. Abbott *et al.* (LIGO Scientific, Virgo, and KAGRA Collaborations), Phys. Rev. Lett. **126**, 241102 (2021).
[10] M. Barriola and A. Vilenkin, Phys. Rev. Lett. **63**, 341 (1989).
[11] C. M. Will, Living Rev. Relativity **17**, 4 (2014).
[12] The LIGO Scientific and the Virgo Collaborations, Phys. Rev. Lett. **116**, 241103 (2016).
[13] The LIGO Scientific and the Virgo Collaborations, Phys. Rev. Lett. **118**, 221101 (2017).
[14] The LIGO Scientific and the Virgo Collaborations, Phys. Rev. Lett. **119**, 141101 (2017).
[15] The LIGO Scientific and the Virgo Collaborations, Astrophys. J. Lett. **851**, L35 (2017).
[16] The LIGO Scientific and the Virgo Collaborations, Phys. Rev. Lett. **119**, 161101 (2017).
[17] The Event Horizon Telescope Collaboration, Astrophys. J. Lett. **930**, L12 (2022).

[18] The Event Horizon Telescope Collaboration, Astrophys. J. **875**, L1 (2019).
[19] K. D. Kokkotas and B. G. Schmidt, Living Rev. Relativity **2**, 2 (1999).
[20] E. Berti, V. Cardoso, and A. O. Starinets, Classical Quantum Gravity **26**, 163001 (2009).
[21] R. A. Konoplya and A. Zhidenko, Rev. Mod. Phys. **83**, 793 (2011).
[22] D. N. Vollick, Phys. Rev. D **69**, 064030 (2004).
[23] M. Banados, Phys. Rev. D **77**, 123534 (2008).
[24] P. Pani, T. Delsate, and V. Cardoso, Phys. Rev. D **85**, 084020 (2012).
[25] P. Pani, V. Cardoso, and T. Delsate, Phys. Rev. Lett. **107**, 031101 (2011).
[26] P. P. Avelino, Phys. Rev. D **85**, 104053 (2012).
[27] J. R. Nascimento, G. J. Olmo, P. J. Porfírio, A. Y. Petrov, and A. R. Soares, Phys. Rev. D **101**, 064043 (2020).
[28] M. Bañados and P. G. Ferreira, Phys. Rev. Lett. **105**, 011101 (2010).
[29] X. Shi and X.-z. Li, Classical Quantum Gravity **8**, 761 (1991).
[30] A. Achucarro, B. Hartmann, and J. Urrestilla, J. High Energy Phys. 07 (2005) 006.
[31] C. Furtado, J. R. Nascimento, A. Y. Petrov, P. J. Porfírio, and A. R. Soares, Phys. Rev. D **103**, 044047 (2021).
[32] A. R. Soares, R. L. L. Vitória, and C. F. S. Pereira, Eur. Phys. J. C **83**, 903 (2023).
[33] B. Toshmatov, O. Rahimov, B. Ahmedov, and A. Ahmedov, Galaxies **9**, 65 (2021).
[34] B. Ahmedov, O. Rahimov, and B. Toshmatov, Universe **7**, 307 (2021).
[35] B. Toshmatov, Phys. Dark Universe **35**, 100992 (2022).
[36] B. F. Schutz and C. M. Will, Astrophys. J. **291**, L33 (1985).
[37] S. Iyer and C. M. Will, Phys. Rev. D **35**, 3621 (1987).
[38] S. Iyer, Phys. Rev. D **35**, 3632 (1987).
[39] R. A. Konoplya, Phys. Rev. D **68**, 024018 (2003).
[40] J. Matyjasek and M. Opala, Phys. Rev. D **96**, 024011 (2017).
[41] R. A. Konoplya, A. Zhidenko, and A. F. Zinhailo, Classical Quantum Gravity **36**, 155002 (2019).
[42] H. Ciftci, R. L. Hall, and N. Saad, J. Phys. A **36**, 11807 (2003).
[43] H. T. Cho, A. S. Cornell, J. Doukas, and W. Naylor, Classical Quantum Gravity **27**, 155004 (2010).
[44] T. Wuthicharn, S. Ponglertsakul, and P. Burikham, Int. J. Mod. Phys. D **31**, 2150127 (2022).
[45] R. G. Daghigh, M. D. Green, J. C. Morey, and G. Kunstatter, Phys. Rev. D **102**, 104040 (2020).
[46] E. W. Leaver, Proc. R. Soc. A **402**, 285 (1985).
[47] P. Pani, Int. J. Mod. Phys. A **28**, 1340018 (2013).
[48] M. Dimitrijević Ćirić, N. Konjik, and A. Samsarov, Phys. Rev. D **101**, 116009 (2020).
[49] C. Gundlach, R. H. Price, and J. Pullin, Phys. Rev. D **49**, 883 (1994).
[50] C. B. M. H. Chirenti and L. Rezzolla, Classical Quantum Gravity **24**, 4191 (2007).
[51] B. Toshmatov, Z. Stuchlík, J. Schee, and B. Ahmedov, Phys. Rev. D **97**, 084058 (2018).
[52] Y. Decanini and A. Folacci, Phys. Rev. D **81**, 024031 (2010).
[53] V. Cardoso, A. S. Miranda, E. Berti, H. Witek, and V. T. Zanchin, Phys. Rev. D **79**, 064016 (2009).
[54] R. A. Konoplya and A. Zhidenko, J. Cosmol. Astropart. Phys. 05 (2017) 050.
[55] B. Toshmatov, Z. Stuchlík, and B. Ahmedov, Phys. Rev. D **98**, 085021 (2018).
[56] B. Toshmatov, Z. Stuchlík, B. Ahmedov, and D. Malafarina, Phys. Rev. D **99**, 064043 (2019).
[57] R. A. Konoplya, Phys. Lett. B **838**, 137674 (2023).